*fluids*

MDPI

*Article*

# Low Reynolds Number Settling of Bent Rods in Quiescent Fluid

**Amirhossein Hamidi [1], Daniel Daramsing [1], Mark D. Gordon [2] and Ronald E. Hanson [1,*]**

[1] Department of Mechanical Engineering, York University, 4700 Keele St., North York, ON M3J 1P3, Canada
[2] Earth and Space Science and Engineering, York University, 4700 Keele St., North York, ON M3J 1P3, Canada
* Correspondence: hansonre@yorku.ca

**Abstract**

This study experimentally investigates the settling behavior of bent (V-shaped and curved) and straight rods in a quiescent fluid at low and finite Reynolds numbers ($Re < 3$). The impact of the rod morphology on the terminal settling velocity and drag coefficient was examined, with a particular focus on V-shaped rods compared to straight rods of the same dimensions (diameter and length) and curved rods of the same dimensions and projected area. The results show that V-shaped rods consistently settle faster than straight rods, with velocity differences influenced by the bend angle. This velocity difference reaches a maximum of 57% for a V-shaped rod with a diameter of 0.50 mm, an aspect ratio of 90, and a bend angle of 45 degrees. When compared to curved rods, V-shaped rods exhibit slightly higher terminal velocities, with a maximum difference of 4% in this study, attributed to differences in mean inclination angles. Furthermore, the drag coefficient trends reflect the interplay between the settling velocity and projected area changes with the rod geometry. A new semi-empirical model with an RMS error of 7.1% was also developed to predict the drag coefficients and terminal velocities of straight and bent rods within the ranges studied. These findings and the model presented underscore the significance of the fibre shape in accurately predicting settling dynamics, with implications for atmospheric transport modeling and industrial applications involving fibrous particles.

**Keywords:** terminal velocity; settling velocity; low Reynolds number; cylindrical rods; bent rods

## 1. Introduction

The morphologies of small fibrous particles can significantly influence their settling velocities in a quiescent fluid. Fibres encountered in natural and industrial settings often deviate from idealized straight cylinders, exhibiting curvature or bending along their axis. For example, microfibres, known to be the most abundant types of airborne microplastics [1,2], can adopt a range of shapes, as found in deposition samples [3–5]. Past simulations of microfibre transport and deposition in the atmosphere have mostly modeled these fibres as volume-equivalent spheres or straight cylindrical rods. However, this can result in the inaccurate prediction of their terminal velocities [3] and long-range transport [6]. Improved modeling that accounts for the fibre shape provides a stronger basis for predicting settling velocities, as required for transport simulations. Moreover, the impact of the fibre geometry extends to diverse applications, such as paper manufacturing [7] and biomedical processes [8].

Various studies have investigated the settling of straight cylindrical particles in quiescent fluids over a wide range of Reynolds numbers (Re)—from the Stokes regime, where inertia is negligible, to low but finite Re, where inertial effects become significant. Henn [9]

Check for updates

Academic Editor: Chongqing Ru

Received: 22 December 2025
Revised: 3 March 2026
Accepted: 7 March 2026
Published: 9 March 2026

**Copyright:** © 2026 by the authors. Licensee MDPI, Basel, Switzerland. This article is an open access article distributed under the terms and conditions of the Creative Commons Attribution (CC BY) license.

developed a theoretical model predicting the terminal velocities of long cylinders within the Stokes regime, achieving agreement within 5% of experimental results for settling glass fibres. Yuan et al. [10] numerically examined the settling of submillimeter microplastic fibres in still water. They found that, within the laminar regime (Re $< 0.1$, where Re is calculated based on the volume-equivalent diameter), Stokes' law ($C_D = 24/\mathrm{Re}$) accurately predicts terminal velocities for fibres with small orientation angles ($\theta < 30^\circ$, where $\theta$ is the angle between the fibre axis and the horizontal). However, for $\theta > 30^\circ$, orientation effects become significant even within this low Reynolds range. Khayat and Cox [11] formulated a model for the hydrodynamic forces on slender bodies of arbitrary cross-section and curvature at low and finite Re using asymptotic expansions in aspect ratio to capture inertial effects. Their approach yielded explicit expressions for the total force and torque exerted on straight bodies, including cylinders. Jayaweera and Mason [12] experimentally measured the terminal velocities and drag coefficients of cylinders in viscous fluids across a broad range of Re. They found that cylinders retain their initial orientations for $\mathrm{Re}_D < 0.01$ (where $\mathrm{Re}_D$ is based on the cylinder diameter) but reorient horizontally for $\mathrm{Re}_D > 0.01$ due to inertial effects, exhibiting the maximum resistance. However, McNown and Malaika [13] reported horizontal orientation at Re $> 0.1$. Kharrouba et al. [14] and Fintzi et al. [15] proposed refined models for the hydrodynamic forces and torques applied to finite cylinders inclined in a uniform flow across viscous to inertial regimes. For $\mathrm{Re}_D < 10$, their correlations outperformed slender-body theory (SBT) [11,16] for both parallel and perpendicular force components, yielding accurate predictions of the total hydrodynamic force and torque under Stokes flow conditions. Finally, Lopez and Guazzelli [17] developed a model for the settling velocities, orientations, and 3D trajectories of fibres in vortical flows accounting for finite inertia. Their results improved upon SBT for finite aspect ratios and moderate Re, but the model remains valid only for Re based on a cylinder half-length greater than unity.

The influence of non-straight geometries on the settling behaviour of cylindrical rods and fibres at low and finite Reynolds numbers has also been widely investigated. Nguyen et al. [18] examined the effects of fibre bending on the terminal velocity through a parameter termed curliness, defined as the ratio of the actual fibre length to its diagonal length. They found that, for fibres longer than 1 mm, increased curliness reduces the settling rate; for example, the terminal velocity of a 2 mm fibre decreases by a factor of 1.75 as curliness increases from 1 to 1.3. Marchetti et al. [19] and Li et al. [20] demonstrated that elastic fibres deform during settling, with their velocities increasing with the elastogravitational number (defined as the ratio of gravitational to bending forces). As this number increases, the fibre shape transitions from slightly bent to V-shaped and eventually to a U shape, with the terminal velocity reaching up to 1.6 times that of a straight fibre [19]. The Reynolds numbers in these experiments, based on the fibre half-length, were below 0.2, indicating negligible inertial effects. During settling, the fibres undergo reorientation and rotation before reaching a stable configuration, leading to oscillations in velocity and coupling between horizontal and vertical motion [20,21]. The settling of rigid U-shaped rods within $0.43 < \mathrm{Re} < 1.78$ was investigated in our recent work [22,23], which showed that such rods adopt oblique orientations at higher Reynolds numbers and smaller middle-arm length ratios, allowing them to settle faster than straight counterparts. Yang et al. [24] studied slender fibres settling in air and found that curved fibres descend more rapidly than straight ones, as their curvature better conforms to streamlines and reduces pressure differentials. They identified the diameter as the most influential parameter on the settling velocity, followed by the fibre length, curvature, and moisture absorption. Using the lattice Boltzmann method, Rong et al. [7] compared straight and curved fibres with an identical aspect ratio and observed that fibres with smaller radii of curvature settle faster and reach the terminal velocity more quickly, with less overshoot. In a recent work, Hamidi

et al. [23,25] investigated the settling of straight and curved rods within $0.03 < \mathrm{Re} < 5$ and found that curvature consistently enhances the settling velocity. A predictive model incorporating the rod aspect ratio, sphericity, and the projected length-to-rod-length ratio was developed, demonstrating improved accuracy over existing correlations when validated against experimental data. Moreover, other studies have shown that non-spherical or irregular particles, such as spheroids [26] and complex-shaped sheets [27,28], exhibit intricate settling behaviour even at low Reynolds numbers without inertial effects. These findings collectively emphasize that the particle geometry, symmetry, and flexibility strongly govern sedimentation dynamics, often producing non-trivial trajectories and reorientations even in the absence of inertia.

The influence of bent geometries, including V-shaped and curved rods, on settling behaviour at low and finite Reynolds numbers has received limited attention in previous studies. The present work examines the terminal velocities and drag coefficients of V-shaped rods and compares them with those of straight rods of identical dimensions (diameter and length) and with curved rods of equivalent dimensions and projected frontal areas. The difference in terminal velocity between the two bent geometries is further interpreted in terms of their morphological distinctions. Building on our recent study of straight and curved rods [25], this work introduces V-shaped geometries and extends the range of curvature indices considered for curved rods. Section 2 describes the experimental setup, materials, and methods. Section 3 presents the results, including terminal velocity and drag coefficient measurements for V-shaped rods, comparative analyses with straight rods, an assessment of velocity differences between V-shaped and curved rods of matching projected areas, and the development of a new semi-empirical model to predict the terminal velocity in straight and bent rods.

## 2. Experimental Setup

This study aims to replicate the range of Reynolds numbers relevant to the atmospheric settling of microfibres. The literature reports the typical dimensions of plastic microfibres from atmospheric depositions, with lengths ranging from 100 to 700 µm [29–31], although a broader range has also been noted [32–34]. While information on the microfibre diameter is less abundant, studies suggest that their aspect ratios range from a few to about 100 [30,35]. Based on these dimensions and the density of typical synthetic microfibres, the Reynolds number for their settling in quiescent air is predicted to be less than 5 when using models by Henn [9] and Hamidi et al. [25]. The Reynolds number is calculated from [25,36]

$$\mathrm{Re} = \frac{\rho_f V_S D_{eq}}{\mu_f}, \tag{1}$$

where $\rho_f$, $V_S$, $D_{eq}$, and $\mu_f$ are the fluid density, rod terminal velocity, diameter of the volumetric-equivalent sphere, and fluid viscosity, respectively. The following subsections elaborate on the materials used in this study, the experimental facility, and the analysis methods.

### *2.1. Materials*

In this study, metal rods were released in a highly viscous fluid to reproduce the Reynolds numbers relevant to the settling of plastic microfibres in the atmosphere. A water–glycerin mixture with a glycerin weight ratio of 90% was selected to achieve the target Reynolds number range, consistent with the methodology of Hamidi et al. [25]. The viscosity of the mixture was measured using a Discovery HR-3 Hybrid Rheometer with a concentric cylinder geometry and calibrated against the N75 Viscosity Standard (Cannon Instruments Company). The average uncertainty of the viscosity measurements was 0.3%,

and temperature-induced variations were corrected using the correlation proposed by Cheng [37].

Aluminum rods with a diameter of 0.51 mm and brass rods with diameters of 0.50 and 1.0 mm were tested, each with dimensional uncertainty of ±0.05 mm. The aluminum rods ($\rho_P = 2710 \pm 66$ kg/m$^3$, where $\rho_P$ denotes the rod density) resulted in very low Reynolds numbers (Re $< 0.1$), while the brass rods ($\rho_P = 8730 \pm 49$ kg/m$^3$) corresponded to higher Reynolds numbers ($0.1 <$ Re $< 2.7$). All rods were cut using a jeweller's saw blade with length uncertainty of ±0.1 mm and polished flat at both ends.

Figure 1 shows a schematic of the rod geometries, and Table 1 lists the properties of the straight and V-shaped rods. The rod diameter ($D_C$) and length ($L_C$) are used to define the aspect ratio ($AR = L_C/D_C$). The V-shaped rods were formed by bending straight rods at their midpoint to a prescribed bend angle ($\alpha$ in Figure 1), ranging from 45° to 135°. The resulting projected length ($L_P$ in Figure 1) was within ±0.1 mm for each $\alpha$ and was calculated from

$$L_P = L_C \times \sin(\alpha/2). \quad (2)$$

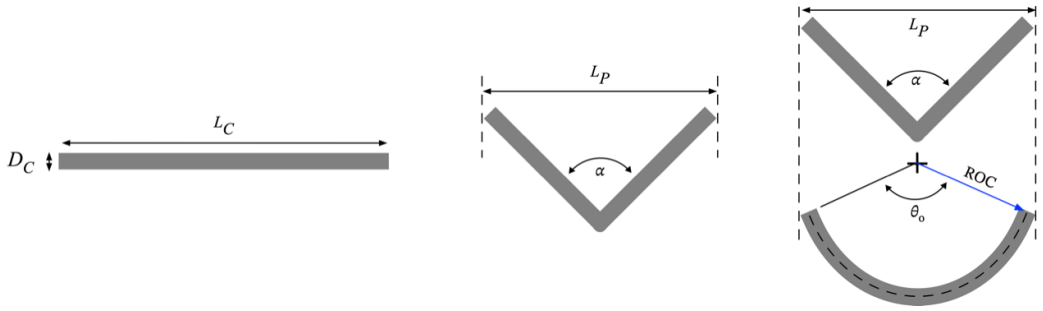


**Figure 1.** Schematic of a straight rod (**left**), a V-shaped rod (**middle**), and a curved rod with the same projected area as the V-shaped rod (**right**). $D_C$, $L_C$, $\alpha$, $\theta_0$, ROC, and $L_P$ indicate the rod diameter, rod length, V-shaped rod bend angle, curved rod arc angle, curved rod radius of curvature, and V-shaped and curved rod projected length, respectively.

**Table 1.** Properties of straight and V-shaped rods.

| Geometry | Material | $\rho_P$ (kg/m$^3$) | $D_C$ (mm) | $AR$ | $\alpha$ (°) | Re (Based on $D_{eq}$) | Re$_L$ (Based on $L_C$) |
|---|---|---|---|---|---|---|---|
| Straight | Brass | $8730 \pm 49$ | $0.50 \pm 0.05$ | 20, 30, 60, 90 | | 0.19–0.38 | 1.21–6.66 |
| Straight | Brass | $8730 \pm 49$ | $1.0 \pm 0.05$ | 10, 20, 30, 45 | | 0.83–1.62 | 3.37–17.87 |
| Straight | Aluminum | $2710 \pm 66$ | $0.51 \pm 0.05$ | 30, 45, 60, 90, 120 | | 0.05–0.09 | 0.39–1.94 |
| V-shaped | Brass | $8730 \pm 49$ | $0.50 \pm 0.05$ | 20, 30, 60, 90 | 45, 70, 90, 110, 135 | 0.21–0.62 | 1.32–10.86 |
| V-shaped | Brass | $8730 \pm 49$ | $1.0 \pm 0.05$ | 10, 20, 30, 45 | 45, 70, 90, 110, 135 | 0.90–2.62 | 3.65–29.01 |
| V-shaped | Aluminum | $2710 \pm 66$ | $0.51 \pm 0.05$ | 30, 45, 60, 90, 120 | 45, 70, 90, 110, 135 | 0.05–0.14 | 0.40–2.99 |

The curved rods were produced with the same diameter, length, and projected area as the V-shaped rods for $D_C = 0.50$ mm. The total length of a curved rod is calculated from

$$L_C = \text{ROC} \times \theta_0, \quad (3)$$

where ROC and $\theta_0$ represent the curved rod's radius of curvature and arc angle, respectively. The projected length for the curved rod can be calculated from

$$L_P = 2\text{ROC} \times \sin(\theta_0/2). \tag{4}$$

By eliminating ROC from Equations (3) and (4), we have

$$L_P\theta_0 - 2L_C\sin(\theta_0/2) = 0. \tag{5}$$

Given the known values of $L_C$ and $L_P$ for a V-shaped rod, the arc angle ($\theta_0$) of a curved rod with an identical diameter, length, and projected area can be obtained from Equation (5). Once $\theta_0$ is determined, the radius of curvature (ROC) is calculated using Equation (3) or (4). In this manner, each curved rod is designed to have the same projected length ($L_P$) as its corresponding V-shaped counterpart. Only curved rods with $\theta_0 < 180°$, i.e., those smaller than a half-circle, are considered in this study. The curvature index, which quantifies the deviation of a curved rod geometry from that of a straight rod [7,24,25], is calculated from

$$C = 1 - \frac{L_P}{L_C}. \tag{6}$$

Substituting Equations (3) and (4) into Equation (6) gives

$$C = 1 - \frac{2\sin(\theta_0/2)}{\theta_0}. \tag{7}$$

As $\theta_0$ varies only between 0 and 180°, the variation in $C$ is limited to between 0 and 0.36. The values of 0 and 0.36 correspond to a straight rod and a half-circle curved rod, respectively. The ratio of $L_P/L_C$, denoted by $\beta$ in this study, can also be determined for a V-shaped rod, with $L_P$ calculated from Equation (2), which results in $\beta = \sin(\alpha/2)$. By equating $\beta$ between the curved and V-shaped rod, we have

$$\beta = \sin(\alpha/2) = 1 - C. \tag{8}$$

Given the range of variation for $C$, $\alpha$ ranges between 80° and 180°. As a result, curved rods with the same dimensions and projected areas as the V-shaped rods were produced only for V-shaped rods with $\alpha = 80°, 85°, 90°, 110°,$ and 135°, $D_C = 0.50$ mm, and $AR = 60$ and 90. Table 2 shows a summary of the parameters of the curved rods, as well as the corresponding V-shaped rods with the same dimensions and projected areas.

**Table 2.** The geometric parameters of the curved rods and the corresponding V-shaped rods with the same projected areas. The rod diameter for all cases in this table is 0.50 mm.

| $AR$ | $\alpha$ (°) | $L_P$ (mm) | $\theta_0$ (°) | ROC (mm) | $C$ | $\beta$ |
|---|---|---|---|---|---|---|
| 60 | 80 | 18.6 | 180 | 9.6 | 0.36 | 0.64 |
| 90 | 80 | 29.3 | 180 | 14.5 | 0.36 | 0.64 |
| 60 | 85 | 20.5 | 169 | 10.2 | 0.32 | 0.68 |
| 90 | 85 | 30.6 | 169 | 15.3 | 0.32 | 0.68 |
| 60 | 90 | 21.2 | 159 | 10.8 | 0.29 | 0.71 |
| 90 | 90 | 31.8 | 159 | 16.2 | 0.29 | 0.71 |
| 60 | 110 | 24.5 | 123 | 13.9 | 0.18 | 0.82 |
| 90 | 110 | 37.3 | 123 | 21.6 | 0.18 | 0.82 |
| 60 | 135 | 27.9 | 78 | 22.8 | 0.08 | 0.92 |
| 90 | 135 | 41.5 | 78 | 32.5 | 0.08 | 0.92 |

### 2.2. Experimental Facility

The experimental facility consists of a settling chamber and a stereoscopic imaging system. As shown in Figure 2, the side and bottom walls of the chamber are constructed from clear acrylic sheets to enable the illumination and visualization of the rod trajectory during settling. The chamber has a square cross-section of 0.25 m × 0.25 m and a height of 1.0 m. It was filled with a water–glycerin mixture containing 90 wt% glycerin. Illumination was provided by two 10 W LED lights positioned behind two perpendicular sides of the chamber. The imaging system includes two monochromatic Kaya Iron 250 CXP cameras (8-bit resolution) fitted with Basler C-mount lenses with a 50 mm focal length, capturing synchronized images from perpendicular views corresponding to the ZY and XY planes, as illustrated in Figure 2. Both side cameras were positioned 0.9 m from the chamber walls. A third camera, equipped with a 25 mm Basler C-mount lens, was mounted beneath the chamber at a distance of 0.60 m from the bottom acrylic wall to record any rotational motion of the rods about the vertical (Y) axis. The vertical field of view of each side camera was 15 cm, while the bottom camera covered the full base area of the chamber. The lower edge of the side cameras' field of view was located 7.5 cm above the bottom wall. All cameras were connected to a computer via a Komodo II four-channel CoaXPress 12 G frame grabber. Image acquisition and synchronization were managed using Vision Point. Because the density and viscosity of the water–glycerin mixture were temperature-sensitive, a T-type thermocouple was used to continuously monitor the temperature at various depths. The measured temperature was consistent within $\pm 0.1^{\circ}$. When not in use, the chamber was sealed to minimize evaporation. The viscosity and density of the mixture were measured throughout the experiments and remained stable. Mixture homogeneity was verified by measuring the viscosities of samples drawn from the top, middle, and bottom of the chamber, which showed a standard-deviation-to-mean ratio of 0.4%.

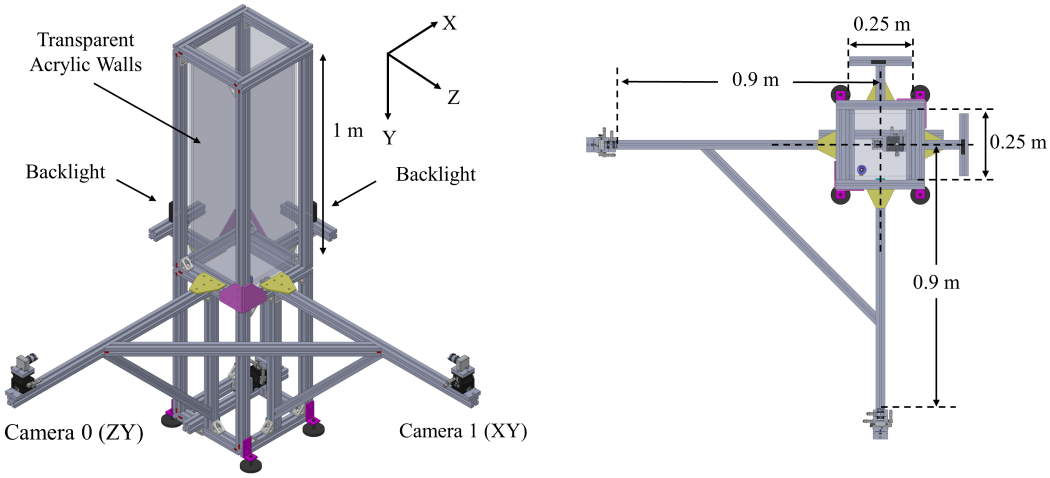


**Figure 2.** Schematic of the experimental setup. The isometric view (**left**) illustrates the tank, camera layout, and backlighting arrangement, while the top view (**right**) details the tank dimensions and camera stand-off distances.

### 2.3. Analysis Methods

Images from the two side cameras were analyzed using a custom MATLAB R2025a script to identify key points of the rod geometry, including the centroid, endpoints, and midpoint, along the fall trajectory. The image processing procedure involved binarization, inversion, and key point detection, as illustrated in Figure 3. Key points were extracted using MATLAB functions *regionprops* and *pgonCorners*. Pixel coordinates from the two side cameras were converted to real-world coordinates via a mapping function similar to that of Soloff et al. [38] and as described in our recent study [25]. The mapping function was

determined using a calibration grid of 59 × 60 dots spaced 2 mm apart, placed at a 45° angle inside the chamber, with corresponding pixel coordinates obtained from the side cameras.

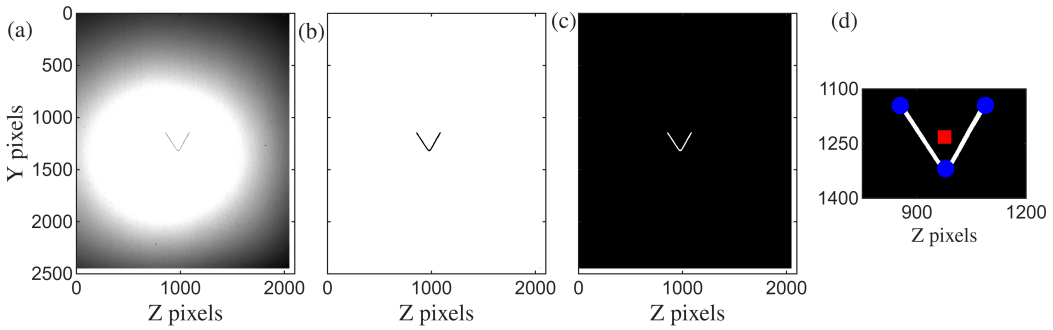


**Figure 3.** Image analysis steps for a single frame of a settling V-shaped rod with $D_C = 0.50$ mm, $AR = 60$, and $\alpha = 90°$: (**a**) original image, (**b**) binarized image, (**c**) inverted image, and (**d**) detected key points of the rod, including the centroid (red square) as well as the two endpoints and the midpoint (blue circles).

The settling velocity was calculated by dividing the vertical displacement of the centroid between consecutive images by the time interval. Variations in settling velocity over the last 15 cm of the trajectory were less than 1% of the average, indicating negligible fluctuations. The terminal velocity was computed as the average velocity over this portion. Wall effects were considered using Brenner's model [39], yielding an average velocity ratio $V_S/V_\infty = 0.98$, where $V_\infty$ denotes the settling velocity in an infinite medium, corresponding to 2% uncertainty. The influence of the bottom wall was assessed using Sano's model [40], giving $V_S/V_\infty \approx 1$, indicating a negligible impact. To account for experimental repeatability and rod manufacturing variations, each drop test was repeated at least five times using a minimum of three different rod samples, and uncertainty of 2% was assumed for each factor. This methodology was also employed to measure the terminal velocity of settling spheres within $\mathrm{Re} < 1$ by Daramsing [41], and a difference of 0.8% was found between the experimental results and Stokes' formula (24/Re).

## 3. Results and Discussion

Straight, V-shaped, and curved rods were dropped into the viscous mixture, and their orientations and terminal velocities were examined. This section presents the results and analysis of these experiments.

### *3.1. Rod Orientation and 3D Trajectory*

As mentioned in Section 2.3, the real-life locations of the V-shaped rod centroid, endpoints, and midpoint were determined using stereo imaging and analysis. Assuming that the centroid of the rod in the first captured frame is at the origin, the locations of these points in the initial frame, as well as the subsequent frames, can be determined. This process enables the determination of the 3D trajectory of the rod fall, as shown in Figure 4. Only every seventh point is displayed for improved visualization in this figure. The 3D trajectories and the images captured from the bottom camera reveal that V-shaped, curved, and straight rods show no spinning motion or horizontal drift once they reach their stable terminal velocity and orientation within the ranges studied. As also observed in previous studies [12,25,42], straight rods consistently orient horizontally upon reaching their terminal velocity within $\mathrm{Re} > 0.1$, irrespective of their initial orientation. A constant orientation and velocity during settling indicate that the rod has reached equilibrium. This stable orientation, and consequently the terminal velocity, does not depend on the entry conditions or initial orientations of the rods and is determined by the balance between

gravitational and inertial torques. At a very low Reynolds number (Re $< 0.1$), where the inertia effects are insignificant, the straight rods retain their initial orientations throughout their fall trajectory [12,13]. In these cases, such as those involving aluminum rods, the rods are dropped with an initial horizontal orientation in the present experiments. As an example, the 3D trajectory of a straight brass rod with $D_C = 0.50$ mm and $AR = 60$, along with the variations in its inclination angle, is shown in Figure 4. The inclination angle is defined as the angle between the rod axis and the horizontal direction. The mean value for the inclination angle is 0.13 degrees for this case, which is within the uncertainty of our measurements. This negligible inclination angle does not cause any changes to the rod drag coefficient or terminal velocity of the straight rods investigated in this study.

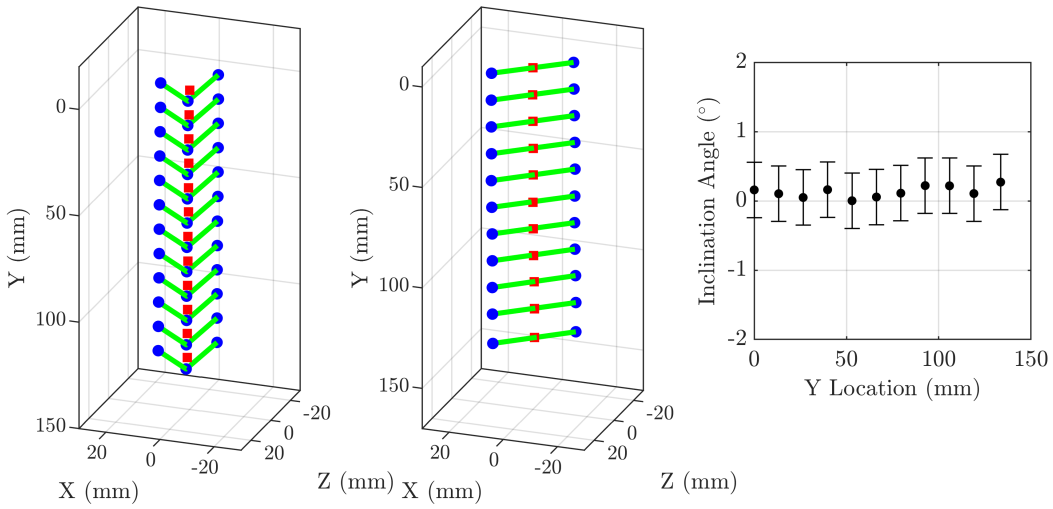


**Figure 4.** The 3D trajectories of a V-shaped rod with $D_C = 0.50$ mm, $AR = 60$, and $\alpha = 90°$ (**left**) and a straight rod with the same diameter and aspect ratio (**middle**). The **right** panel shows the variations in the inclination angle of the straight rod with the vertical location.

The V-shaped rods consistently orient such that their apex is pointed downward. A similar orientation is also observed for the curved rods, as reported in [7,16,25]. This behaviour of V-shaped rods can be explained by the balance between inertial torque and gravitational torque. Due to the symmetric geometry of a V-shaped rod, the two arms exhibit mirror symmetry with respect to a vertical axis passing through the bottom vertex of the V. Each inclined arm experiences an inertial torque that tends to reorient it horizontally, but, because the arms are identical and symmetrically angled in opposite directions, the torques have equal magnitude and opposite direction. This results in their cancellation, producing no net inertial torque capable of reorienting the particle. Consequently, the V-shaped rods settle with a constant orientation, with the bottom vertex remaining at the lowest point due to the impact of gravitational torque, within the Reynolds number range investigated in this study. However, if they are dropped with a different orientation, the imbalance between the inertial torques applied to the two arms and the gravitational torque causes an initial reorientation during settling until it reaches the constant stable orientation. The same rationale can be applied to curved rods, which can be assumed to be composed of an infinite number of inclined cylindrical rod elements, symmetrically arranged about a central axis. As a result, the curved rods also settle stably, maintaining an orientation that maximizes their projected area perpendicular to the direction of motion.

### 3.2. Terminal Velocity

Figure 5 illustrates the variations in the V-shaped rod's terminal velocity with the geometric parameters, compared to straight rods. The left plot shows the terminal velocity as a function of the aspect ratio, with results shown only for a bend angle of $\alpha = 45°$ for clarity; similar trends were observed for other bend angles. Across all conditions, V-shaped rods consistently settle faster than straight rods of the same dimensions. The maximum relative difference, 57%, occurs for $D_C = 1.0$ mm, $AR = 45$, and $\alpha = 45°$, within the ranges investigated. As with straight rods [12,25], the terminal velocities of V-shaped rods increase with the rod diameter and aspect ratio. Variations diminish at high aspect ratios due to the reduced influence of the two rod ends. In a previous work [25], we showed that a straight rod's terminal velocity asymptotically approaches that of an infinite cylinder, as predicted by Khalili and Liu [43] or Huner and Hussey [44], for $AR > 90$. This asymptotic behaviour was also demonstrated in Jayaweera and Manson's study [12].

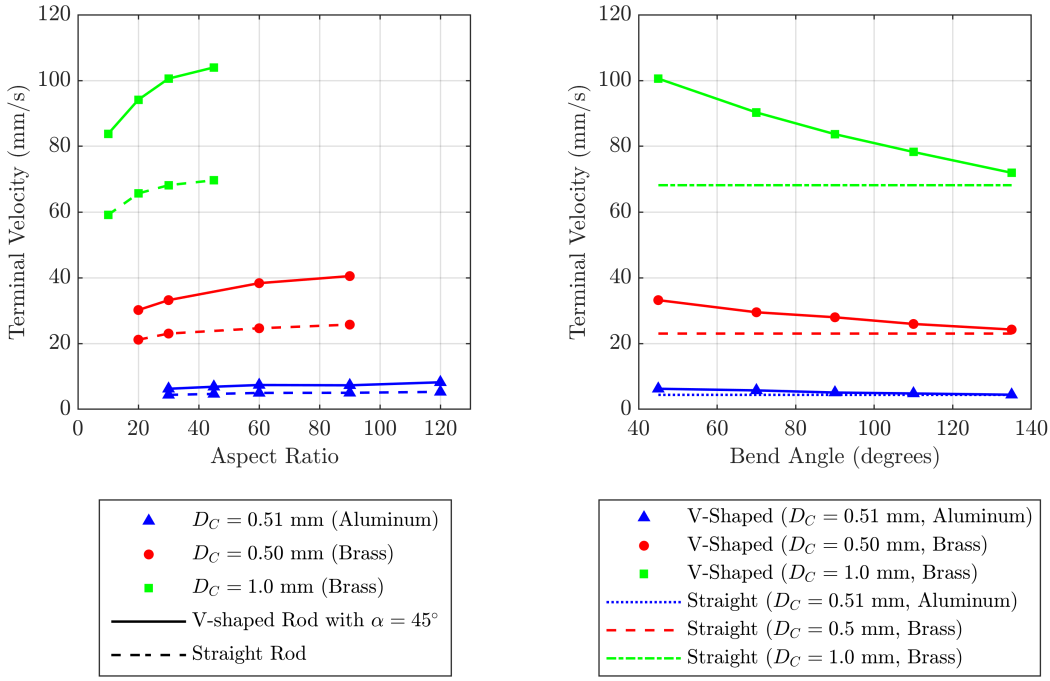


**Figure 5.** Terminal velocities of V-shaped rods and their comparison with straight rods. The **left** plot shows the variations in terminal velocity with the aspect ratio for different diameters for $\alpha = 45°$. The **right** plot shows the variations in terminal velocity with the bend angle for different diameters for $AR = 30$.

The right plot in Figure 5 shows the effect of the bend angle on the terminal velocity for rods with $AR = 30$; similar trends were observed for other aspect ratios. Larger bend angles (45° to 135°) lead to lower terminal velocities. At larger angles, the rate of velocity decrease slows, and the terminal velocity approaches that of a straight rod of the same diameter and aspect ratio. Specifically, increasing $\alpha$ from 45° to 70° reduces the velocity by 13%, whereas the reduction is only 7% for $\alpha = 110°$ to 135°. This behaviour reflects the greater sensitivity of the terminal velocity to end effects at smaller bend angles, when the arms are more vertically oriented.

Figure 6 compares the terminal velocities of V-shaped rods with those of curved rods with an identical diameter, aspect ratio, and projected area, across different curvature indices (given by $C$ in Equation (6)) for $D_C = 0.50$ mm and $AR = 60$ and 90. Within the investigated ranges, V-shaped rods settle slightly faster than curved rods, with the relative difference increasing with $C$, reaching a maximum of 4% at $C = 0.36$ (the maximum feasible value for a half-circle). The velocity ratio is almost the same for both aspect ratios, suggest-

ing that it depends only on the curvature index. This indicates that, within the investigated Reynolds number range, the projected morphology rather than the overall rod length primarily governs the relative settling enhancement between the two bent geometries.

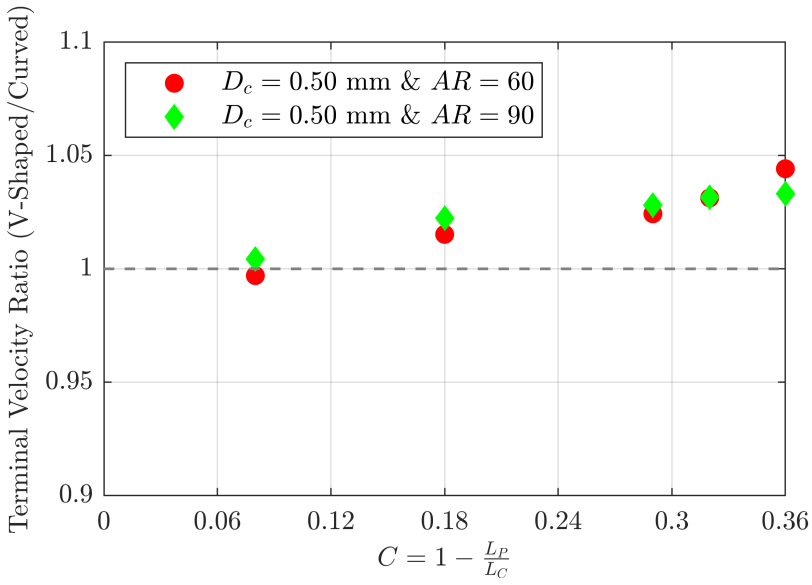


**Figure 6.** The ratio of the V-shaped rod's terminal velocity to that of a curved rod with the same projected area.

The increase in the terminal velocity of the V-shaped rod compared to the curved rod with the same dimensions and projected area can be explained by comparing the "mean inclination angle" of the curved rod with that of the V-shaped rod. According to Figure 7, the inclination angle of an arbitrary element of the curved rod at point A (dS) can be defined as the angle between the tangential line to the curved rod at this point and the vertical line. This angle is denoted by $\gamma$ and can be calculated from

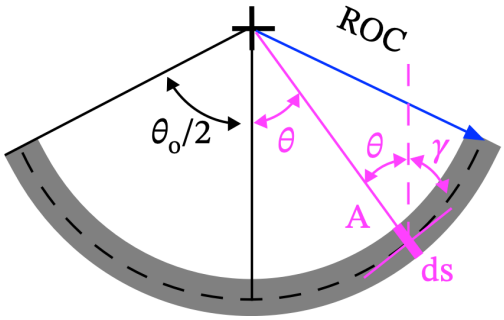


**Figure 7.** Definition of inclination angle for a curved rod.

$$\gamma = \frac{\pi}{2} - \theta \tag{9}$$

Therefore, the mean inclination angle for the entire curved rod ($\overline{\gamma}$) is calculated from

$$\overline{\gamma} = \frac{1}{(\mathrm{ROC})(\theta_0/2)} \int_0^{\theta_0/2} (\frac{\pi}{2} - \theta)\, \mathrm{ds}, \tag{10}$$

where $\mathrm{ds} = (\mathrm{ROC})\mathrm{d}\theta$. Equation (10) results in $\overline{\gamma} = (\pi/2) - (\theta_0/4)$. Considering equal total and projected lengths between V-shaped and curved rods, the V-shaped rod's inclination angle $\alpha_0 = \alpha/2$ relates to the curved rod's arc angle ($\theta_0$) as

$$\alpha_0 = \sin^{-1}\left(\frac{2\sin(\theta_0/2)}{\theta_0}\right). \quad (11)$$

The ratio of the curved rod's mean inclination angle to that of the V-shaped rod ($\overline{\gamma}/\alpha_0$) is plotted versus $\theta_0$ in Figure 8. This figure shows that $\overline{\gamma}$ is consistently larger than $\alpha_0$, indicating a more horizontally aligned mean orientation for the curved rod compared to the V-shaped rod with the same dimensions and projected area. This difference in mean orientation explains why V-shaped rods settle faster than corresponding curved rods with the same dimensions and projected areas. Therefore, even when the projected area is held constant, differences in how local elements are distributed relative to the vertical direction produce measurable changes in drag and settling velocity.

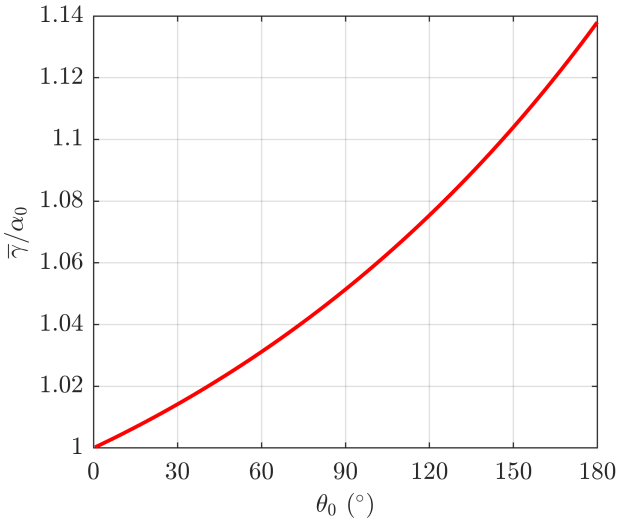


**Figure 8.** Ratio of the mean inclination angle of the curved rod ($\overline{\gamma}$) to that of the V-shaped rod ($\alpha_0$) versus the curved rod arc angle ($\theta_0$).

### *3.3. Drag Coefficient*

The variations in the V-shaped rod's drag coefficient ($C_D$) with the Reynolds number for different diameters, aspect ratios, and bend angles are shown in Figure 9. The Reynolds number is calculated based on the diameter of a volumetric-equivalent sphere (Equation (1)), and the drag coefficient is defined as in [25,36,45].

In this section, the variations in the V-shaped rod's drag coefficient with the Reynolds number for different rod diameters, aspect ratios, and bend angles are discussed. The Reynolds number is calculated based on the diameter of a volumetric-equivalent sphere using Equation (1). The drag coefficient is calculated from [25,36,45]

$$C_D = \frac{(\rho_P - \rho_f)g(\pi/4)D_C^2 L_C}{0.5\rho_f V_S^2 A_P}, \quad (12)$$

where $\rho_P$ and $g$ are the rod density and gravity acceleration, respectively. $A_P$ equals $L_C D_C \sin(\alpha/2)$ for the V-shaped rods and $L_C D_C$ for the straight rods, given their orientations when they reach the terminal velocity, as discussed in Section 3.1.

As shown in Figure 9, for both V-shaped and straight rods, an increasing aspect ratio for a given diameter increases Re due to the larger volumetric-equivalent sphere and higher terminal velocity, consistent with the straight rod results in [25]. Changing the rod diameter or material shifts the Reynolds number range. For example, aluminum rods with $D_C = 0.51$ mm cover $0.05 < \mathrm{Re} < 0.14$, brass rods with $D_C = 0.50$ mm cover $0.19 < \mathrm{Re} < 0.62$, and brass rods with $DC = 1.0$ mm cover $0.83 < \mathrm{Re} < 2.62$. Furthermore, for the same diameter and aspect ratio, Re increases as the bend angle decreases due to a

higher terminal velocity (Section 3.2). Figure 9 shows that $C_D$ decreases with an increasing rod aspect ratio and diameter. The resulting increase in the diameter of a volumetric-equivalent sphere and the higher terminal velocity result in a lower drag coefficient, as also occurs for Stokes' law for a sphere ($C_D = 24/\mathrm{Re}$). Deviations from Stokes' law are due to the difference in particle geometry (cylindrical rods compared to a spherical geometry at the same Reynolds number). In our related work [25], we demonstrated that straight rods' drag coefficients at high aspect ratios ($AR > 90$) converge to predictions from 2D cylinder models [43,44]. The effect of the bend angle on $C_D$ is also shown in Figure 9. For a given diameter and aspect ratio, decreasing $\alpha$ from 180° (straight rod) to approximately 90° reduces the drag coefficient, as the increase in terminal velocity dominates over changes in projected area according to Equation (12). For $\alpha < 90°$, further decreasing the bend angle increases $C_D$, as changes in projected area outweigh terminal velocity effects. This non-monotonic behaviour reflects the trade-off between $V_S^2$ and $A_P$ in Equation (12). This result highlights that the bend angle influences drag not through a single geometric parameter but through the coupled effects of the projected area and velocity-dependent inertial contributions.

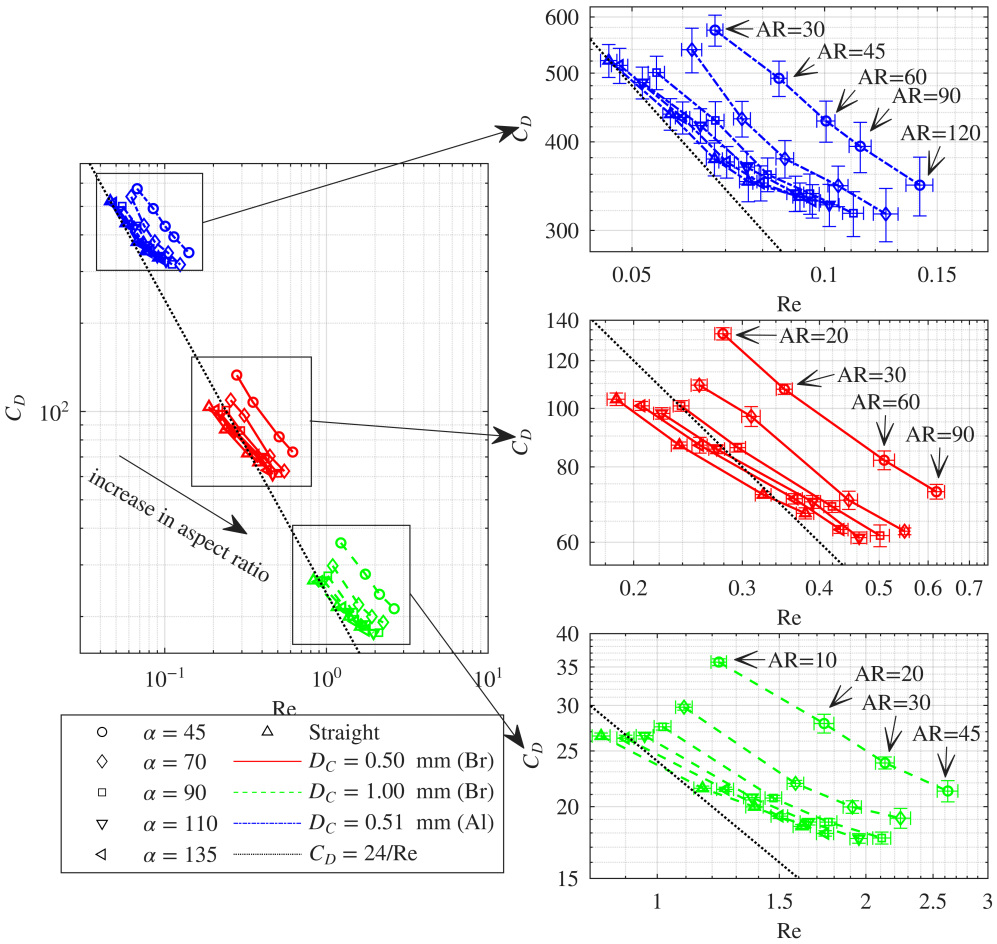


**Figure 9.** Variations in drag coefficient with Reynolds number for V-shaped and straight rods, considering different rod diameters, aspect ratios, and bend angles. The aspect ratios are shown for one bend angle; the same aspect ratios apply to the other bend angles. The dotted line represents the drag coefficient calculated using Stokes' law for a sphere. "Al" refers to aluminum, and "Br" refers to brass.

### 3.4. Model Development

A new semi-empirical model to predict the drag coefficients and terminal velocities of bent and straight rods is proposed in this section. This model is based on the framework proposed in our recent work [25], which was developed for straight and curved rods and expanded upon an earlier model developed by Song et al. [36]. A comprehensive physical interpretation of this model was presented in our recent work [25]. To explain briefly here, by introducing the rod aspect ratio ($AR$) and rod projected-length-to-total-length ratio ($\beta$) into the Song model and removing $S$, defined as the ratio of the volumetric-equivalent sphere's projected area to that of the particle, our new model for straight and curved rods was derived. Upon introducing the aspect ratio into the model, the error decreases from 22% to 6.8% when compared to the straight rod data points [25]. Furthermore, the term $S$ was eliminated from Song's model [36] to adapt it for straight, curved, and V-shaped rods, as these geometries maintain a constant horizontal orientation during settling at low Reynolds numbers upon reaching their stable terminal velocities. The model was compared to all straight and curved rod results in our recent study, and an RMS error of 6.8% was achieved [25]. This model showed an improvement over the previous models in the literature for straight rods, including those developed for a variety of microplastic particle geometries [46–48], as well as those developed for cylindrical geometries based on slender body theory [11,14–16]. The general form of this model is

$$C_D = \frac{24}{\mathrm{Re}(AR^c \phi^d \beta^e)}(1 + a\mathrm{Re})^b, \tag{13}$$

where $\phi$ denotes the rod sphericity, defined as the ratio of the surface area of a volume-equivalent sphere to that of the rod. In this study, this general form of the model is employed for bent (curved and V-shaped) and straight rods. According to Figure 9, $C_D$ varies non-linearly with the bend angle for V-shaped rods, with $\beta$ consequently defined as $L_P/L_C$. Specifically, as $\beta$ increases, $C_D$ generally decreases within the range $0.38 < \beta < 0.71$ (corresponding to $45^\circ < \alpha < 90^\circ$) and increases within $0.71 < \beta < 0.92$ (corresponding to $90^\circ < \alpha < 135^\circ$). It should also be noted that changes in $\beta$ influence the Reynolds number used in the model (Equation (13)) due to its effect on the terminal velocity. Therefore, the overall impact of $\beta$ on $C_D$ also depends on how Re varies with $\beta$. To capture the effect of $\beta$ on $C_D$ for bent rods, proportionality of $C_D \propto 1/\beta^e$ is assumed. The coefficients of $a$, $b$, $c$, $d$, and $e$ should be determined such that the model can be applied for bent and straight rods. Based on the definition of $\beta$, $\beta = 1$ for straight rods and $\beta < 1$ for bent rods. Therefore, for straight rods, this new model does not differ from our previous model applied to straight and curved rods [25]. This requires the use of the previous values for the coefficients of $a$, $b$, $c$, and $d$, meaning that $a = 0.25$, $b = 0.96$, $c = 1.20$, and $d = 4.38$. However, the coefficient $e$ should be determined in such a way that the model aligns with both types of bent rods—curved and V-shaped. By fitting the resulting model to the experimental observations for V-shaped rods as well as curved rods from this study (Table 2) and our previous work [25], the value of 0.65 is determined. As a result, our new model is given by Equation (13), with the coefficients listed in Table 3.

**Table 3.** The coefficients used in our new model (Equation (13)).

| *a* | *b* | *c* | *d* | *e* |
|---|---|---|---|---|
| 0.25 | 0.96 | 1.20 | 4.38 | 0.65 |

Comparison with Experiments and Other Models

The terminal velocities of the V-shaped rods settling in a water–glycerin mixture with a glycerin weight ratio of 90% at a temperature of 21 °C were calculated using the model developed in Section 3.4. The calculated results were compared with the experimental data points obtained in this study in Figure 10, and an RMS error of 7.9% was obtained. The experimental terminal velocities shown in this figure were corrected using Brenner's correction factor [39] to account for the effects of the bounded medium in which the rod settled. Our model can be applied to the settling of straight rods if $\beta = 1$, which will be the same as in the previous model for straight rods developed in our recent related work [25]. The results of the model for straight rods were compared to the experimental results in our recent study [25], and an RMS error of 6.8% was obtained. Furthermore, a comprehensive comparison between our new model for straight rods and other models developed for the settling of straight cylinders was provided in our recent study [25].

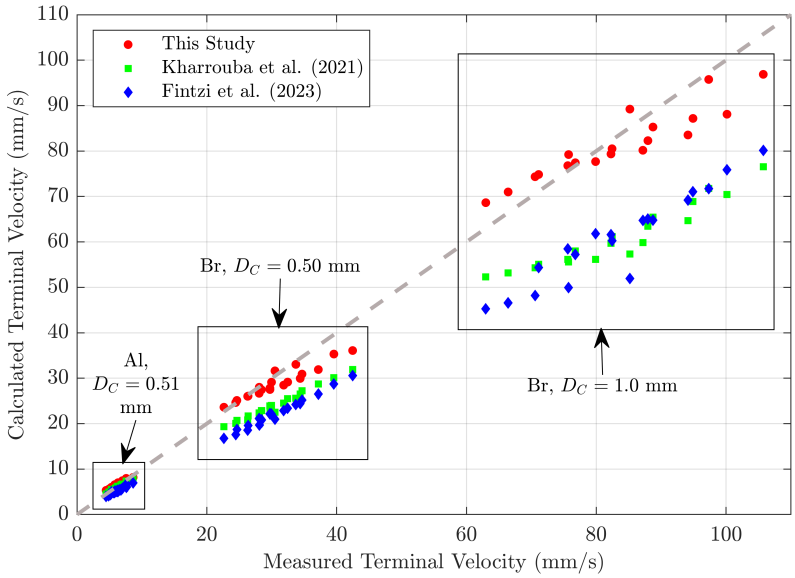


**Figure 10.** A comparison of the V-shaped rods' terminal velocities, as calculated using the new model developed in this study (Equation (13)), with the measured terminal velocities. The results of two other models for inclined cylinders relative to the flow, by Kharrouba et al. [14] and Fintzi et al. [15], are also compared to the experimental data. The dashed line represents the equivalence between the calculated and measured data points. "Al" refers to aluminum, and "Br" refers to brass.

The terminal velocities of the V-shaped rods investigated in this study were also compared with those of two other models described by Kharrouba et al. [14] and Fintzi et al. [15], which were developed for the aerodynamic forces applied to an inclined cylinder at low Reynolds numbers. For this comparison, it was assumed that a V-shaped rod is composed of two inclined cylinders, with an inclination angle of $\alpha/2$ relative to the vertical direction, and the total drag force opposite to the vertical fall direction was calculated. The horizontal lift forces applied to the two inclined cylinders balance each other out due to the symmetry of the V-shaped rod geometry relative to the middle vertical axis. Therefore, the only component of the aerodynamic force affecting the settling of a V-shaped rod is the vertical drag force acting on each inclined arm. Considering the mentioned drag force, as well as the gravity and buoyancy forces exerted on the V-shaped rods, the terminal velocities were determined and compared with the experimental results in Figure 10. As can be seen, there are larger discrepancies between the experimental data and both the Kharrouba model [14] and the Fintzi model [15]. The RMS errors of the Kharrouba model [14] and the Fintzi model [15] when compared to the measured terminal

velocities of the V-shaped rods are 19.4% and 23.5%, respectively. The assumption of two individual inclined rods instead of a V-shaped rod neglects the interactions between the two rods when they are joined at one endpoint, which may account for the discrepancy. As illustrated in Figure 10, the velocities predicted by the Kharrouba and Fintzi models underestimate the terminal velocities.

The model proposed in this study can also be applied to curved rods with arc angles smaller than 180 degrees. The curvature index ($C$) in our recent study [25] ranged between zero and 0.25, while, with the newly added curved rods mentioned in Table 2, the curvature index range is extended to $0 < C < 0.36$ in the present study. As discussed in Section 2.1, this range covers the entire feasible curvature index range for all curved rods with $\theta_0 < 180°$. The terminal velocities of the curved rods calculated from our previous model [25] and the model proposed in this study (Equation (13)) are compared with the experimental data in Figure 11. As is evident from this figure, the data points associated with our new model are closer to the dashed line that equates the measured and calculated values. The RMS error of our previous model for all curved rods investigated in the previous [25] and current studies is 6.8%, whereas the RMS error of our new model for the same rods is 4.1%. The primary reason for the difference between these two models for the curved rods is that our previous model is valid within $C < 0.25$, while the valid curvature index range in our new model is extended to $C < 0.36$ due to the inclusion of newly studied curved rods (Table 2). The RMS error of our previous model for $0.25 < C < 0.36$, which falls outside the valid range for this model, is 11.8%, whereas it is only 4.6% in our new model. Consequently, the new model proposed in this study (Equation (13)) can be applied to straight, V-shaped, and curved rods within $0.03 < \mathrm{Re} < 5$, $3 < AR < 120$, and $0.64 < \beta < 1$ with an RMS error of 7.1%. Additionally, this model can be utilized for V-shaped rods with the aforementioned ranges of Re and $AR$ and $0.38 < \beta$.

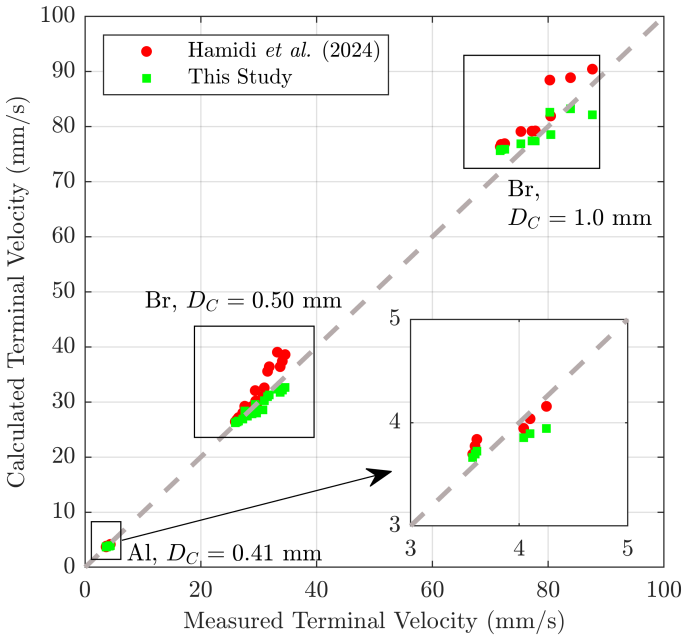


**Figure 11.** Comparison of the terminal velocities of curved rods settling in a 90% glycerin mixture, as predicted by the model developed in our recent study [25] and the new model proposed in this study (Equation (13)), with measured values. "Al" means aluminum and "Br" means brass. The inset zooms in on the area covered by the results of aluminum rods with $D_C = 0.41$ mm.

## 4. Conclusions

The settling of straight, V-shaped, and curved rods in a quiescent fluid at low and finite Reynolds numbers was experimentally investigated, revealing the significant influence of the rod morphology on the terminal velocity and orientation. V-shaped rods consistently attain higher terminal velocities than equivalent straight rods of the same diameter and aspect ratio. At Reynolds numbers above 0.1, where inertial effects are significant, straight rods orient horizontally at the terminal velocity, whereas V-shaped rods are oriented with their center of gravity at the lowest point. Curved rods were designed with the same diameter, aspect ratio, and projected area as the V-shaped rods, spanning geometries from slightly curved to semi-circular. Comparisons show that V-shaped rods settle slightly faster than the corresponding curved rods, with the relative velocity difference increasing with the curvature index and reaching a maximum of 4% for semi-circular shapes. This difference is attributed to the larger mean inclination angle of the curved rods relative to vertical, compared with V-shaped rods of identical dimensions and projected areas, highlighting the importance of inclination in settling dynamics. Regarding drag, the V-shaped rod's drag coefficient decreases as the rod bends from a straight configuration to a 90° angle, driven by the dominant effect of an increased terminal velocity. For bend angles below 90°, the drag coefficient increases as changes in projected area become more significant than velocity effects. A new semi-empirical model was also derived to predict the drag coefficients and terminal velocities of bent and straight rods within $0.64 < \beta < 1$ for curved and $0.38 < \beta < 1$ for V-shaped rods, with $0.03 < \mathrm{Re} < 5$ and $3 < AR < 120$. The root mean square error of this model, when compared to experimental data points, is 7.1%. In addition to its validity for V-shaped bent rod geometries, our new model provides a more comprehensive valid range of curvature indices for curved rods ($C < 0.36$), where the parameter $C$ defines curved rods up to semi-circular geometries. Overall, these results emphasize the dependence of rod or fibre settling behaviour on the geometry, with the presented non-dimensional results and the model providing practical guidance for estimating the terminal velocities of both straight and bent elongated particles.

**Author Contributions:** Conceptualization, R.E.H. and M.D.G.; methodology, A.H. and D.D.; software, A.H. and D.D.; validation, A.H. and D.D.; formal analysis, A.H. and D.D.; investigation, A.H.; resources, A.H., D.D., R.E.H. and M.D.G.; data curation, A.H. and D.D.; writing—original draft preparation, A.H.; writing—review and editing, R.E.H. and M.D.G.; visualization, A.H. and D.D.; supervision, R.E.H. and M.D.G.; project administration, R.E.H. and M.D.G.; funding acquisition, R.E.H. and M.D.G. All authors have read and agreed to the published version of the manuscript.

**Funding:** This project is funded in part by the Northern Contaminants Program (CIRNAC, M-61) and the Government of Canada (ECCC, Grants and Contributions Award GCXE21S030).

**Institutional Review Board Statement:** Not applicable.

**Informed Consent Statement:** Not applicable.

**Data Availability Statement:** All data supporting the findings of this study are available upon reasonable request to the authors.

**Conflicts of Interest:** The authors declare no conflicts of interest.

## Nomenclature

The following nomenclature is used in this manuscript:

| | |
|---|---|
| $D_{eq}$ | Volume-equivalent diameter (mm) |
| $D_C$ | Rod diameter (mm) |
| $L_C$ | Rod length (mm) |
| $AR$ | Rod aspect ratio (-) |

| | |
|---|---|
| $\alpha$ | Bend angle (°) |
| $V_S$ | Terminal velocity (mm/s) |
| $C_D$ | Drag coefficient (-) |
| Re | Reynolds number based on the volume-equivalent diameter (-) |
| $\mathrm{Re}_D$ | Reynolds number based on the rod diameter (-) |
| $\mathrm{Re}_L$ | Reynolds number based on the rod length (-) |
| $\rho_f$ | Fluid density (kg/m$^3$) |
| $\mu_f$ | Fluid dynamic viscosity (Pa.s) |
| $\rho_p$ | Rod density (kg/m$^3$) |
| $A_P$ | Rod projected area (mm$^2$) |
| $L_P$ | Rod projected length (mm) |
| $C$ | Curvature index (-) |
| $\beta$ | Projected-length-to-total-length ratio (-) |
| $\theta_0$ | Arc angle (°) |
| ROC | Radius of curvature (°) |
| $\overline{\gamma}$ | Mean inclination angle of the curved rod (°) |
| $\alpha_0$ | Mean inclination angle of the V-shaped rod (°) |

## References


1. Fox, S.; Stefánsson, H.; Ásbjörnsson, E.J.; Peternell, M.; Wanner, P.; Sturkell, E.; Konrad-Schmolke, M.; Zlotskiy, E. Physical characteristics of microplastic particles and potential for global atmospheric transport: A meta-analysis. *Environ. Pollut.* **2024**, *342*, 122938. [CrossRef]
2. Martynova, A.; Genchi, L.; Laptenok, S.P.; Cusack, M.; Stenchikov, G.L.; Liberale, C.; Duarte, C.M. Atmospheric microfibrous deposition over the Eastern Red Sea coast. *Sci. Total Environ.* **2024**, *907*, 167902. [CrossRef]
3. Xiao, S.; Cui, Y.; Brahney, J.; Mahowald, N.M.; Li, Q. Long-distance atmospheric transport of microplastic fibres influenced by their shapes. *Nat. Geosci.* **2023**, *16*, 863–870. [CrossRef]
4. Bourzac, K. Scientists race to study microplastic pollution in the atmosphere. *Chemical and Engineering News*, 20 February 2022; Volume 100.
5. Gasperi, J.; Wright, S.L.; Dris, R.; Collard, F.; Mandin, C.; Guerrouache, M.; Langlois, V.; Kelly, F.J.; Tassin, B. Microplastics in air: Are we breathing it in? *Curr. Opin. Environ. Sci. Health* **2018**, *1*, 1–5. [CrossRef]
6. Ward, E.; Gordon, M.; Hanson, R.; Jantunen, L.M. Modelling the effect of shape on atmospheric microplastic transport. *Atmos. Environ.* **2024**, *326*, 120458. [CrossRef]
7. Rong, X.; Qi, D.; He, G.; Zhu, J.; Scott, T. Single curved fiber sedimentation under gravity. *Comput. Math. Appl.* **2008**, *55*, 1560–1567. [CrossRef]
8. Farhaj, S.; Conway, B.R.; Ghori, M.U. Nanofibres in drug delivery applications. *Fibers* **2023**, *11*, 21. [CrossRef]
9. Henn, A. Calculation of the stokes and aerodynamic equivalent diameters of a short reinforcing fiber. *Part. Part. Syst. Charact.* **1996**, *13*, 249–253. [CrossRef]
10. Yuan, F.; Dai, C.; Ying, Y.; Wang, D.; Yang, X.; Du, J.; Yu, W. Prediction of the settlement of submillimeter microplastic fibers in still water. *Environ. Technol. Innov.* **2025**, *37*, 103951. [CrossRef]
11. Khayat, R.; Cox, R. Inertia effects on the motion of long slender bodies. *J. Fluid Mech.* **1989**, *209*, 435–462. [CrossRef]
12. Jayaweera, K.; Mason, B.J. The behaviour of freely falling cylinders and cones in a viscous fluid. *J. Fluid Mech.* **1965**, *22*, 709–720. [CrossRef]
13. McNown, J.S.; Malaika, J. Effects of particle shape on settling velocity at low Reynolds numbers. *EOS Trans. Am. Geophys. Union* **1950**, *31*, 74–82.
14. Kharrouba, M.; Pierson, J.L.; Magnaudet, J. Flow structure and loads over inclined cylindrical rodlike particles and fibers. *Phys. Rev. Fluids* **2021**, *6*, 044308. [CrossRef]
15. Fintzi, N.; Gamet, L.; Pierson, J.L. Inertial loads on a finite-length cylinder embedded in a steady uniform flow. *Phys. Rev. Fluids* **2023**, *8*, 044302. [CrossRef]
16. Cox, R. The motion of long slender bodies in a viscous fluid: Part 1. General theory. *J. Fluid Mech.* **1970**, *44*, 791–810. [CrossRef]
17. Lopez, D.; Guazzelli, E. Inertial effects on fibers settling in a vortical flow. *Phys. Rev. Fluids* **2017**, *2*, 024306. [CrossRef]
18. Nguyen, T.H.; Kieu-Le, T.C.; Tang, F.H.; Maggi, F. Controlling factors of microplastic fibre settling through a water column. *Sci. Total Environ.* **2022**, *838*, 156011. [CrossRef]
19. Marchetti, B.; Raspa, V.; Lindner, A.; Du Roure, O.; Bergougnoux, L.; Guazzelli, É.; Duprat, C. Deformation of a flexible fiber settling in a quiescent viscous fluid. *Phys. Rev. Fluids* **2018**, *3*, 104102. [CrossRef]

20. Li, L.; Manikantan, H.; Saintillan, D.; Spagnolie, S.E. The sedimentation of flexible filaments. *J. Fluid Mech.* **2013**, *735*, 705–736. [CrossRef]
21. Du Roure, O.; Lindner, A.; Nazockdast, E.N.; Shelley, M.J. Dynamics of flexible fibers in viscous flows and fluids. *Annu. Rev. Fluid Mech.* **2019**, *51*, 539–572. [CrossRef]
22. Hamidi, A.; Gordon, M.D.; Jantunen, L.M.; Hanson, R.E. Settling of U-shaped rods at low Reynolds numbers. *Phys. Fluids* **2025**, *37*, 073377. [CrossRef]
23. Hamidi, A. Low Reynolds Number Settling of Cylindrical Rods with Various Geometries in a Quiescent Fluid. Ph.D. Thesis, York University, Toronto, ON, Canada, 2025.
24. Yang, X.; Wang, Y.; Li, Y.; Cao, Y.; Zhou, Y.; Huang, Y. Experimental research on the settling property of slender fiber particles under the influence of multiple factors. *Powder Technol.* **2022**, *405*, 117543. [CrossRef]
25. Hamidi, A.; Daramsing, D.; Gordon, M.D.; Jantunen, L.M.; Hanson, R.E. Straight and curved cylindrical rods settling in quiescent fluid with application to atmospheric microplastics. *Exp. Fluids* **2024**, *65*, 81. [CrossRef]
26. Bhowmick, T.; Seesing, J.; Gustavsson, K.; Guettler, J.; Wang, Y.; Pumir, A.; Mehlig, B.; Bagheri, G. Inertia induces strong orientation fluctuations of nonspherical atmospheric particles. *Phys. Rev. Lett.* **2024**, *132*, 034101. [CrossRef]
27. Huseby, E.; Gissinger, J.; Candelier, F.; Pujara, N.; Verhille, G.; Mehlig, B.; Voth, G. Helical ribbons: Simple chiral sedimentation. *Phys. Rev. Fluids* **2025**, *10*, 024101. [CrossRef]
28. Vaquero-Stainer, C.; Miara, T.; Juel, A.; Pihler-Puzović, D.; Heil, M. U-shaped disks in Stokes flow: Chiral sedimentation of a non-chiral particle. *J. Fluid Mech.* **2024**, *999*, A71. [CrossRef]
29. Zhang, Y.; Kang, S.; Allen, S.; Allen, D.; Gao, T.; Sillanpää, M. Atmospheric microplastics: A review on current status and perspectives. *Earth-Sci. Rev.* **2020**, *203*, 103118. [CrossRef]
30. Wright, S.; Ulke, J.; Font, A.; Chan, K.L.A.; Kelly, F.J. Atmospheric microplastic deposition in an urban environment and an evaluation of transport. *Environ. Int.* **2020**, *136*, 105411. [CrossRef]
31. Allen, S.; Allen, D.; Phoenix, V.; Le Roux, G.; Jiménez, P.; Simonneau, A.; Binet, S.; Galop, D. Atmospheric transport and deposition of microplastics in a remote mountain catchment. *Nat. Geosci.* **2019**, *12*, 339–344. [CrossRef]
32. Bergmann, M.; Mützel, S.; Primpke, S.; Tekman, M.; Trachsel, J.; Gerdts, G. White and wonderful? Microplastics prevail in snow from the Alps to the Arctic. *Sci. Adv.* **2019**, *5*, eaax1157. [CrossRef]
33. Li, Y.; Lu, Q.; Xing, Y.; Liu, K.; Ling, W.; Yang, J.; Yang, Q.; Wu, T.; Zhang, J.; Pei, Z.; et al. Review of research on migration, distribution, biological effects, and analytical methods of microfibers in the environment. *Sci. Total Environ.* **2023**, *855*, 158922. [CrossRef] [PubMed]
34. Mbachu, O.; Jenkins, G.; Pratt, C.; Kaparaju, P. A new contaminant superhighway? A review of sources, measurement techniques and fate of atmospheric microplastics. *Water Air Soil Pollut.* **2020**, *231*, 85. [CrossRef]
35. Dris, R.; Gasperi, J.; Saad, M.; Mirande, C.; Tassin, B. Synthetic fibers in atmospheric fallout: A source of microplastics in the environment? *Mar. Pollut. Bull.* **2016**, *104*, 290–293. [CrossRef]
36. Song, X.; Xu, Z.; Li, G.; Pang, Z.; Zhu, Z. A new model for predicting drag coefficient and settling velocity of spherical and non-spherical particle in Newtonian fluid. *Powder Technol.* **2017**, *321*, 242–250. [CrossRef]
37. Cheng, N. Formula for the viscosity of a glycerol-water mixture. *Ind. Eng. Chem. Res.* **2008**, *47*, 3285–3288. [CrossRef]
38. Soloff, S.; Adrian, R.; Liu, Z. Distortion compensation for generalized stereoscopic particle image velocimetry. *Meas. Sci. Technol.* **1997**, *8*, 1441. [CrossRef]
39. Brenner, H. Effect of finite boundaries on the Stokes resistance of an arbitrary particle. *J. Fluid Mech.* **1962**, *12*, 35–48. [CrossRef]
40. Sano, O. Mobility of a small sphere in a viscous fluid confined in a rigid circular cylinder of finite length. *J. Phys. Soc. Jpn.* **1987**, *56*, 2713–2720. [CrossRef]
41. Daramsing, D.V. Settling Velocity of Straight and Curved Rods at Low Reynolds Numbers in a Quiescent Fluid. Master's Thesis, York University, Toronto, ON, Canada, 2023.
42. Roy, A.; Hamati, R.; Tierney, L.; Koch, D.; Voth, G. Inertial torques and a symmetry breaking orientational transition in the sedimentation of slender fibres. *J. Fluid Mech.* **2019**, *875*, 576–596. [CrossRef]
43. Khalili, A.; Liu, B. Stokes' paradox: Creeping flow past a two-dimensional cylinder in an infinite domain. *J. Fluid Mech.* **2017**, *817*, 374–387. [CrossRef]
44. Huner, B.; Hussey, R. Cylinder drag at low Reynolds number. *Phys. Fluids* **1977**, *20*, 1211–1218. [CrossRef]
45. Bagheri, G.; Bonadonna, C. On the drag of freely falling non-spherical particles. *Powder Technol.* **2016**, *301*, 526–544. [CrossRef]
46. Zhang, J.; Choi, C.E. Improved Settling Velocity for Microplastic Fibers: A New Shape-Dependent Drag Model. *Environ. Sci. Technol.* **2022**, *56*, 962–973. [CrossRef]

47. Yu, Z.; Yang, G.; Zhang, W. A new model for the terminal settling velocity of microplastics. *Mar. Pollut. Bull.* **2022**, *176*, 113449. [CrossRef]
48. Goral, K.D.; Guler, H.; Larsen, B.E.; Carstensen, S.; Christensen, E.D.; Kerpen, N.B.; Schlurmann, T.; Fuhrman, D.R. Settling velocity of microplastic particles having regular and irregular shapes. *Environ. Res.* **2023**, *228*, 115783. [CrossRef] [PubMed]

**Disclaimer/Publisher's Note:** The statements, opinions and data contained in all publications are solely those of the individual author(s) and contributor(s) and not of MDPI and/or the editor(s). MDPI and/or the editor(s) disclaim responsibility for any injury to people or property resulting from any ideas, methods, instructions or products referred to in the content.